High-speed, high-resolution optical coherence tomography retinal imaging with a frequency-swept laser at 850 nm

V. J. Srinivasan, R. Huber, I. Gorczynska, and J. G. Fujimoto

Department of Electrical Engineering and Computer Science and Research Laboratory of Electronics Massachusetts Institute of Technology, Cambridge, Massachusetts 02139, USA

J. Y. Jiang, P. Reisen, and A. E. Cable

Thorlabs, Inc., Newton, New Jersey 07860, USA

High-speed, high-resolution optical coherence tomography (OCT) imaging of the human retina is demonstrated using a frequency-swept laser at 850 nm. A compact external cavity semiconductor laser design, optimized for swept-source ophthalmic OCT, is described. The laser enables an effective 16 kHz sweep rate with >10 mm coherence length and a tuning range of $\sim$35 nm full width at half-maximum, yielding an axial resolution of <7 μm in tissue. © 2007 Optical Society of America
OCIS codes: 110.4500, 140.3600, 170.3880.

Optical coherence tomography (OCT) is a noninvasive imaging modality that generates cross-sectional images of tissue architectural morphology with high axial resolution.[1] One of the most important clinical applications of OCT to date has been ophthalmology.[2] Recent work in the field of ophthalmic OCT has shown that spectral/Fourier domain detection methods[3,4] enable OCT imaging with dramatically improved speed and sensitivity over conventional time domain methods.[5–7] The improved performance enables enhanced visualization of retinal pathologies.[8] However, there are several limitations to spectral/Fourier domain OCT detection. First, spectral/Fourier domain OCT utilizes a high-speed camera and spectrometer, which increases system complexity and cost. Second, because of spectrometer and camera resolution limits, sensitivity changes dramatically as a function of axial position or imaging depth.[5,9,10] Finally, camera readout rates and spectrometer losses limit system speed and sensitivity. Swept-source OCT has a similar speed/sensitivity advantage to spectral/Fourier domain OCT, but it overcomes many of the aforementioned limitations. In particular, swept-source OCT has the potential to scale to higher imaging speeds with higher detection efficiency, improved sensitivity, and reduced complexity.

Recently, swept-source OCT retinal imaging was demonstrated at 1050 nm and 18,800 axial scans per second, with 14 μm axial resolution in tissue.[11] In addition, swept-source OCT at 850 nm and 43,500 axial scans per second with 10 μm axial resolution in tissue was demonstrated in microscopy applications.[12] Studies demonstrated that 1050 nm can image deeper structures, such as the choroid. In addition, safe exposure levels are higher for 1050 nm than for 850 nm. However, all clinical studies and instruments to date are based on 850 nm wavelengths. In addition, water absorption below 1000 nm and above 1100 nm limits the usable bandwidth to $\sim$100 nm at

1050 nm, placing limits on axial image resolution. Therefore there is considerable interest in retinal imaging at 850 nm. In this Letter, we demonstrate OCT retinal imaging using an external cavity tunable semiconductor laser at 850 nm. Imaging is performed at 16,000 axial scans per second with <7 μm resolution in tissue.

Recent experimental[13] and theoretical[14] work on rapidly tunable lasers suggests that shorter cavity lengths enable improved power and instantaneous linewidth at high tuning speeds. The laser used in this study has a single-pass cavity length of 15 cm, corresponding to 1 GHz longitudinal mode spacing. The cavity has a folded geometry and contains a semiconductor optical amplifier, collimating lens, half-wave plate, and frequency tunable filter, as shown in Fig. 1(A). The filter consists of a 1700 line/mm reflection grating mounted on an 8 kHz resonant galvanometer, a focusing lens, and a
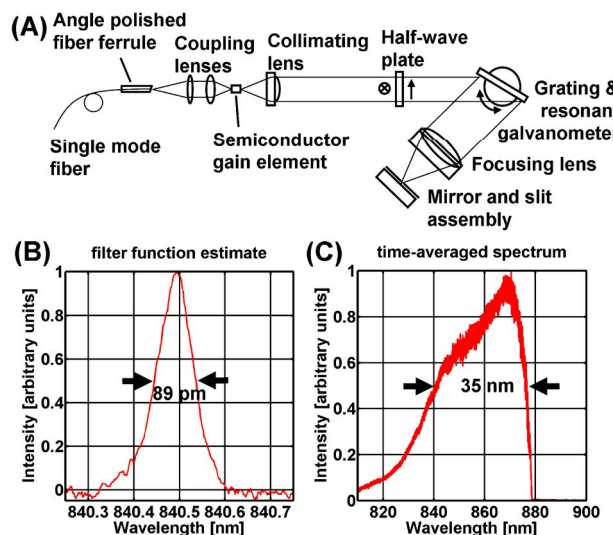
Fig. 1. (Color online) (A) Schematic of frequency-swept laser at 850 nm. (B) Estimate of intracavity filter function. (C) Time-averaged spectrum.

mirror/slit assembly. The elliptical mode from the semiconductor gain element is collimated by a 3.1 mm aspheric lens and is oriented so that the major axis of the elliptical collimated beam is in the plane of Fig. 1(A), which is perpendicular to the grating lines, in order to illuminate the maximum number of grating lines. A half-wave plate between the collimating lens and the grating rotates the polarization of light emitted by the gain element to achieve maximum grating diffraction efficiency. The diffracted light is focused onto a mirror with a 10 μm slit by a 16 mm achromat lens. The choice of slit width produces a trade-off between maximizing spectral filtering to generate a narrow instantaneous linewidth (smaller slit) versus reducing cavity loss and dynamic tuning loss to maximize output power (larger slit). As the grating angle is changed by the galvanometer, different wavelengths are selected. The sinusoidal drive amplitude for the galvanometer is set so that the sinusoid is sufficiently linear over the bandwidth of the semiconductor amplifier, resulting in a duty cycle of ~50%. The width of the filter function is estimated at 840.5 nm as 0.089 nm (38 GHz) FWHM by measuring the stationary linewidth of the laser output when the gain element is driven with a current that is well below the lasing threshold.[15] The estimated filter function is shown in Fig. 1(B) after subtraction of background amplified spontaneous emission. Approximately 38 longitudinal cavity modes are contained within the FWHM of this filter function estimate. The extra-cavity facet of the semiconductor element, with an estimated reflectivity of 20%, serves as the output coupler. The output is collimated by a 4.5 mm focal length aspheric lens and coupled into a single-mode fiber by a 15.4 mm focal length aspheric lens. The fiber-coupled average output power is 2.5 mW at an 80 mA injection current. The time-averaged fiber-coupled spectrum is shown in Fig. 1(C) with a resolution of 0.04 nm.

Retinal imaging is performed using a pair of galvanometer scanning mirrors and optics that relay image the scan plane of the beam onto the subject's pupil. The average power at the cornea is 400 μW, which is consistent with ANSI safety recommendations for pulsed laser exposure. The spot size at the cornea is 1.2 mm FWHM. Dual-balanced detection is performed using a circulator and an 80 MHz balanced receiver. A dispersion-balanced Mach–Zehnder interferometer with a delay of 5 mm, corresponding to a temporal frequency of ~15 MHz, is used to calibrate the frequency sweep. The two fringe traces (the OCT trace and the calibration trace) are acquired simultaneously at 50 MHz by using a 14 bit analog-to-digital (A/D) converter. For online processing and real-time display, wavelength to frequency recalibration is performed using a fast nearest neighbor check algorithm described previously.[13] Recalibration, fast Fourier transformation, display, and data streaming to hard disk for continuous acquisition are performed at a speed of 32 frames per second (512 axial scans per frame). For optimal imaging depth, recalibration is performed offline, using a digital oscilloscope to
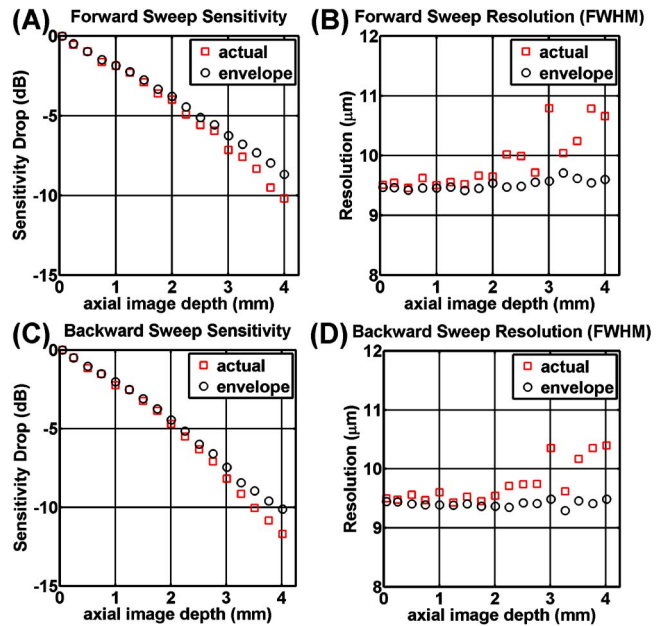
Fig. 2. (Color online) Sensitivity drop and resolution in air as a function of imaging depth in air for both (A), (B) forward and (C), (D) backward sweeps.

sample the two traces. The oscilloscope has higher A/D rates and enables larger imaging depths than the 50 MHz data acquisition system. For offline recalibration, the phase of the Mach–Zehnder calibration trace, which is proportional to the instantaneous frequency of the laser, is obtained by Hilbert transformation. A sixth-order polynomial fit is performed on the Mach–Zehnder phase function. Spline interpolation performed on the OCT trace by using the fitted phase function to obtain samples that are evenly spaced in frequency. Fast Fourier transformation yields the axial reflectance profile. The maximum sensitivity is 96 dB using the Hilbert transform recalibration method and 93 dB using the fast nearest neighbor check algorithm.

Figure 2 shows the measured sensitivity and resolution in air as a function of imaging depth in air for the forward (decreasing frequency) and backward (increasing frequency) sweeps. Forward and backward sweeps have different properties due to nonlinear effects and carrier dynamics. The squares show the sensitivity and resolution values obtained by Fourier transformation of the recalibrated OCT fringe traces at different imaging depths. The circles show the values obtained by Fourier transformation of the envelopes of the recalibrated OCT fringe traces. The sensitivity and resolution values obtained by using the envelope account for changes in the interference spectrum amplitude and shape at different depths but do not account for recalibration errors or residual dispersion that may cause phase errors. To the extent that phase errors are minimized, the sensitivity and resolution values computed by using the envelope (circles) should agree with the actual measured values (squares). The imaging depth, defined as the position where the sensitivity drop is 6 dB, is ~2.5 mm in air. Phase errors cause degradation in resolution past a 3 mm imaging depth.

A high-definition 6 mm image (2048 axial scans, 0.125 s acquisition) of the normal human macula is shown in Fig. 3(A), with a zoom of the foveal region [Fig. 3(B)]. All major intraretinal layers are visible, including the external limiting membrane.[16] A high-definition 4 mm image (2048 axial scans, 0.125 s) across the optic nerve head is shown in Fig. 3(C). Finally, Fig. 3(D) shows a virtual *en face* image of the optic nerve head at the depth of the lamina cribrosa, which was created from a dense 3D OCT data set (512 frames×512 axial scans per frame) and acquired over a 4 mm square region in 16 s. The location of the *en face* image is shown as a black line in Fig. 3(C), and the location of the cross-sectional image in Fig. 3(C) is shown as a white line on the *en face* image [Fig. 3(D)]. The virtual *en face* image was generated in a plane parallel to the plane defined by the termination of the retinal pigment epithelium. The improved sensitivity performance and imaging range of swept-source OCT enables the visualization of deeper structures.

In conclusion, swept-source OCT retinal imaging is demonstrated at 16,000 axial scans per second with an axial resolution of <7 μm in the retina. Maximum imaging depth is determined by the laser coherence length, and good sensitivity and resolution performance at a 4 mm depth are achieved using high-bandwidth data acquisition. By contrast, spectral/Fourier domain detection has a limited imaging depth for a given resolution, which is determined by the Nyquist criterion and the number of camera pix-els. Detection in swept-source OCT is performed with a pair of photodiodes, which have higher efficiency than spectrometers. By further decreasing the laser cavity length and using faster scanning, improvements in speed should be possible without sacrificing power or coherence length. Using the current laser, speeds would eventually be limited by resonant galvanometer technology; however, higher speeds should be possible using other designs. Since swept-source OCT uses photodiodes and high-speed A/Ds, it can operate at higher speeds than spectral/Fourier domain OCT, which uses line-scan CCD cameras. These results suggest that swept-source OCT can achieve performance comparable with or better than that of spectral/Fourier domain OCT for ophthalmic applications.

Fig. 3. (A) High-definition macular image with a zoomed image (B). (C) High-definition optic nerve head image. (D) Virtual image of the lamina cribrosa, created from 3D OCT data. NFL, nerve fiber layer; GCL, ganglion cell layer; IPL, inner plexiform layer; INL, inner nuclear layer; OPL, outer plexiform layer; ONL, outer nuclear layer; ELM, external limiting membrane; IS / OS, photoreceptor inner segment / outer segment junction; PR OS, photoreceptor outer segments; RPE, retinal pigment epithelium; CH, choroid; ONH, optic nerve head.

References

1. D. Huang, E. A. Swanson, C. P. Lin, J. S. Schuman, W. G. Stinson, W. Chang, M. R. Hee, T. Flotte, K. Gregory, C. A. Puliafito, and J. G. Fujimoto, Science **254**, 1178 (1991).
2. M. R. Hee, J. A. Izatt, E. A. Swanson, D. Huang, J. S. Schuman, C. P. Lin, C. A. Puliafito, and J. G. Fujimoto, Arch. Ophthalmol. (Chicago) **113**, 325 (1995).
3. G. Häusler and M. W. Lindner, J. Biomed. Opt. **3**, 21 (1998).
4. A. F. Fercher, C. K. Hitzenberger, G. Kamp, and S. Y. Elzaiat, Opt. Commun. **117**, 43 (1995).
5. R. Leitgeb, C. K. Hitzenberger, and A. F. Fercher, Opt. Express **11**, 889 (2003).
6. J. F. de Boer, B. Cense, B. H. Park, M. C. Pierce, G. J. Tearney, and B. E. Bouma, Opt. Lett. **28**, 2067 (2003).
7. M. A. Choma, M. V. Sarunic, C. Yang, and J. Izatt, Opt. Express **11**, 2183 (2003).
8. U. Schmidt-Erfurth, R. A. Leitgeb, S. Michels, B. Povazay, S. Sacu, B. Hermann, C. Ahlers, H. Sattmann, C. Scholda, A. F. Fercher, and W. Drexler, Invest. Ophthalmol. Visual Sci. **46**, 3393 (2005).
9. N. A. Nassif, B. Cense, B. H. Park, M. C. Pierce, S. H. Yun, B. E. Bouma, G. J. Tearney, T. C. Chen, and J. F. de Boer, Opt. Express **12**, 367 (2004).
10. M. Wojtkowski, V. J. Srinivasan, T. H. Ko, J. G. Fujimoto, A. Kowalczyk, and J. S. Duker, Opt. Express **12**, 2404 (2004).
11. E. C. W. Lee, J. F. de Boer, M. Mujat, H. Lim, and S. H. Yun, Opt. Express **14**, 4403 (2006).
12. H. Lim, J. F. de Boer, B. H. Park, E. C. W. Lee, R. Yelin, and S. H. Yun, Opt. Express **14**, 5937 (2006).
13. R. Huber, M. Wojtkowski, K. Taira, J. G. Fujimoto, and K. Hsu, Opt. Express **13**, 3513 (2005).
14. A. Bilenca, S. H. Yun, G. J. Tearney, and B. E. Bouma, Opt. Lett. **31**, 760 (2006).
15. R. Huber, M. Wojtkowski, J. G. Fujimoto, J. Y. Jiang, and A. E. Cable, Opt. Express **13**, 10523 (2005).
16. W. Drexler, U. Morgner, R. K. Ghanta, F. X. Kärtner, J. S. Schuman, and J. G. Fujimoto, Nat. Med. **7**, 502 (2001).